Exciton spectra and the microscopic structure of self-assembled porphyrin nanotubes

Vlaming, S. M.; Augulis, R.; Stuart, M. C. A.; Knoester, J.; van Loosdrecht, P. H. M.

Published in:
Journal of Physical Chemistry B

DOI:
10.1021/jp808235c

Publication date:
2009

Exciton Spectra and the Microscopic Structure of Self-Assembled Porphyrin Nanotubes

S. M. Vlaming,[†] R. Augulis,[†] M. C. A. Stuart,[‡] J. Knoester,*[,†] and P. H. M. van Loosdrecht[†]

Zernike Institute for Advanced Materials, University of Groningen, Nijenborgh 4, 9747 AG Groningen, The Netherlands, and Groningen Biomolecular Sciences and Biotechnology Institute, University of Groningen, Nijenborgh 4, 9747 AG Groningen, The Netherlands

Received: September 16, 2008; Revised Manuscript Received: December 11, 2008

The optical properties of tubular aggregates formed by self-assembly of zwitterionic meso-tetra(4-sulfonatophenyl)porphyrin ($TPPS_4$) molecules are studied through a combination of experimental and theoretical techniques. The interest in these systems, with diameters of 18 nm and lengths extending up to micrometers, derives from their strong interaction with light and their similarity to natural light-harvesting systems for photosynthesis. The absorption and linear dichroism spectra are obtained in the spectral region from 300 to 750 nm, which includes the exciton bands deriving from the molecular *B* (Soret) as well as the *Q* transitions. We demonstrate that a Frenkel exciton model which takes into account the four dominant molecular excited states (B_x, B_y, Q_x, and Q_y) provides a good global fit to the experimental spectra. From comparison between theory and experiment, we propose a detailed molecular structure within the nanotube.

Introduction

Self-assembled aggregates of organic dye molecules possess unique linear and nonlinear optical properties and display intriguing excitation energy transport phenomena. They are of fundamental interest as model materials to study the nature and the dynamics of excitons in molecular systems of reduced dimensionality. The extraordinary optical properties of molecular aggregates are to a large extent governed by exciton delocalization, transport, and relaxation phenomena. Moreover, molecular aggregates, in particular those of porphyrin derivatives, resemble light-harvesting complexes found in natural photosynthetic systems,[1−5] making them attractive as model materials for studies of fundamental photophysical processes occurring in biological systems as well as for practical applications as building blocks for artificial light energy harvesting and transport systems. Reaching a better understanding of the structural and functional properties of aggregates plays a central role in tuning the self-assembly process and finding desired structures with specific functions.

Among the most prominent examples of aggregates occurring in nature are the chlorosomes of green bacteria,[3,6,7] the structure and properties of which can be closely simulated in artificial model systems—tubular aggregates obtained through self-assembly of, for example, synthetic bacteriochlorophyll derivatives[5,8] or carbocyanine chromophores with amphiphilic sidegroups.[9−13] A number of other porphyrin derivatives, such as $TPPS_2$ (bi(4-sulfonatophenyl)diphenylporphyrin) and $TPPS_3$ (tri(4-sulfonatophenyl)phenylporphyrin),[14] TCPP (tetra(4-carboxyphenyl)porphyrin),[15] $TPPS_4$ (tetra(4-sulfonatophenyl)porphyrin),[16,17] or a mixture of $TPPS_4$ and SnTPyP (Sn(IV) tetra(4-pyridyl)porphyrin),[18] form aggregates of tubular morphology as well. However, in this paper, we will focus solely on the tubular $TPPS_4$ aggregates, because of their high stability and reproducibility of their structural and optical properties.

Due to their unique structural and functional characteristics, $TPPS_4$ nanotubes are promising candidates for various applications in molecular nanotechnology. For example, $TPPS_4$ nanotubes may serve as templates for the formation of composite metallic nanostructures.[19] Recently, photoconductivity and light-induced current generation in $TPPS_4$ aggregates were reported,[20] which may lead to aggregate-based systems for light sensing and harvesting.

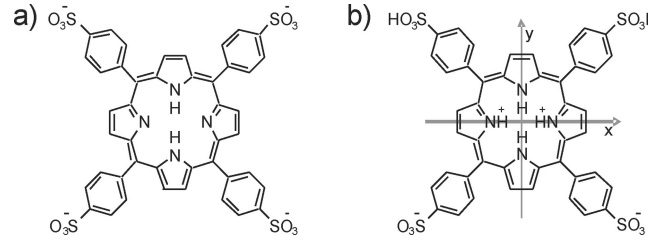

Figure 1. Structure of $TPPS_4$. (a) In pH 7 aqueous solution. (b) Zwitterionic form in pH 1 aqueous solution. B_x, B_y, Q_x, and Q_y transition dipole orientations are indicated by arrows.

$TPPS_4$ is a water-soluble tetrapyrrolic dye (Figure 1a). In neutral to basic aqueous solutions, $TPPS_4$ has four negatively charged sulfonate groups. The resulting electrostatic repulsion limits the possibilities of the molecules to self-assemble. With increasing acidity (starting from pH $\approx$ 4), two additional protons bind to nitrogen atoms at the center of the porphyrin macrocycle, inducing a positive charge density in this region. At even higher acidity (pH 1−2), two additional protons bind to two of the SO_3^- groups and screen their negative charge. The resulting new zwitterionic species (Figure 1b) form J-aggregates, as is evident from the appearance of new absorption bands in the optical spectra.[21−23] Specifically, the monomeric absorption peak at around 434 nm (*B* or, so-called, Soret band) and peaks in the range of 500−650 nm (*Q* bands) transform into much narrower red-shifted peaks at 490 and 709 nm, respectively, which has been attributed to the appearance of extended excited states[21−23] shared by a number of $TPPS_4$ monomers.

The structure of $TPPS_4$ aggregates is stabilized by ionic interactions, and the $\pi-\pi$ interactions between the porphyrin rings. Specifically, the negatively charged SO_3^- side groups of each $TPPS_4$ monomer are positioned above or below the

* E-mail: j.knoester@rug.nl.
[†] Zernike Institute for Advanced Materials.
[‡] Groningen Biomolecular Sciences and Biotechnology Institute.

10.1021/jp808235c CCC: $40.75
Published on Web 02/04/2009

positively charged centers of porphyrin rings of the neighboring molecules. As a result, the formation of threadlike or planar structures of a tiled nature for these aggregates has been suggested.[24−26] Two different zwitterionic forms of $TPPS_4$ monomers can occur, i.e. with the charged side groups on either adjacent or opposite sides of the porphyrin ring. For the zwitterion with oppositely placed SO_3^- groups, a threadlike structure can easily be envisaged.[24−26] There is no trivial way to extend this to a higher-dimensional aggregate, however, the experimental evidence shows that large tubular aggregates are formed.[16,17] The adjacent form of the zwitterion, on the other hand, does support a planar stacking straightforwardly and can thus result in the creation of tubular aggregates. Although the absorption spectra of aggregates formed by $TPPS_4$, $TPPS_3$, $TPPS_{2a}$ (adjacent form), and $TPPS_{2op}$ (opposite form) look similar,[27] the morphology of $TPPS_{2a}$ and $TPPS_{2op}$ aggregates differs drastically.[14] The $TPPS_{2a}$ forms rodlike structures, similar to the ones formed by $TPPS_4$, while the aggregates $TPPS_{2op}$ do not exhibit any regular features. On the basis of this evidence, we single out the zwitterion of $TPPS_4$ with two adjacent charged sulfonate groups as the building block of the aggregates.

Small angle X-ray scattering and atomic force microscopy (AFM) observations have been applied to determine the morphology of the $TPPS_4$ aggregates. Both techniques reveal that $TPPS_4$ monomers, at sufficiently high acidity ($pH \approx 1-2$), aggregate into long (up to several micrometers) cylindrical structures, with a radius of approximately 9 nm.[16,17] While these techniques allow for a good estimate of the dimensions of the tubules, they lack the spatial resolution to determine the microscopic arrangement of the monomers on the cylindrical surface. The fact that the wall thickness of the tubules, estimated by AFM[17,28,29] and cryo-electron microscopy (cryo-EM) experiments reported later in this paper, is 2−2.5 nm, strongly suggests that the tube walls contain no more than a single layer of monomers. $TPPS_4$ is soluble in water, and it is thus not surprising that its aggregates are hygroscopic. Under ambient conditions, it is to be expected that the aggregates can be coated with a layer of condensed water, possibly within the tube as well. AFM measurements in vacuum indeed yield a diminished aggregate thickness.[30] A single-walled nanotubule model is also supported by ab initio and molecular dynamics simulations.[31] The monomers in the aggregate are nonplanar and asymmetrical, namely, two adjacent pyrrole rings are nearly in plane with the porphyrin macrocycle, while the other two are tilted out of plane in opposite directions by a considerable degree. The asymmetry of the monomers leads to the formation of curved molecular threads, which form helices of approximately 20 nm in diameter. Although the molecular dynamics simulations in ref 31 were performed with a one-dimensional thread, the main conclusions apply for a two-dimensional case—the asymmetry of the monomers leads to ring or spirallike threads or equivalently a rolled two-dimensional lattice.

In spite of the considerable understanding of the morphology reported above, a more precise assessment of the molecular arrangement of the $TPPS_4$ nanotubes and its relation to their optical properties remains an issue that needs further investigation. In this paper, we address these issues by combining the data of cryo-electron microscopy and steady state polarization-resolved spectroscopy with numerical simulations of absorption and linear dichroism spectra. We show that a Frenkel exciton model that takes into account the four dominant monomeric transitions (B_x, B_y, Q_x, and Q_y) with appropriate parameters, yields a good global fit of the experimental spectra, allowing us to propose a molecular structure of the nanotubes with greater precision than available hitherto.

This paper is organized as follows. After introducing the experimental methods in the section Materials and Methods, the experimental data are presented in the section Experimental Results. In the section Model, the structural model is introduced, as well as the Frenkel exciton Hamiltonian used to simulate the experimental spectra. The generic results of this type of model for the exciton states and the spectra are discussed, and the incorporation of disorder is addressed. In the section Comparison to Experiment, the full numerical results and the comparison between theory and experiment are presented. Finally, the results are summarized and conclusions are drawn in the section Conclusions. Several details of the theory are addressed in the Appendix.

Materials and Methods

Preparation of $TPPS_4$ Aggregates. Solutions of meso-tetra(4-sulfonatophenyl)porphyrin tetrasodium salt ($TPPS_4$) were prepared by dissolving $TPPS_4$ (Frontier Scientific, Logan, UT) in Milli-Q grade water with an addition of NaOH to keep the pH above 7, which greatly improves solubility. Afterward, the stock solutions, containing 10^{-2} M of $TPPS_4$, were diluted down to $10^{-5}-10^{-3}$ M by adding a pH = 1 aqueous solution of HCl, inducing aggregation. The aggregation process occurs on a time scale of hours to even days for low concentration solutions (10^{-5} M or less), whereas for high concentration solutions (10^{-3} M), it occurs on a time scale of seconds. The samples were left to aggregate at room temperature for at least 24 h, an ample amount of time for the concentrations used in our experiments. No notable spectroscopic differences were observed between solutions in the range $2 \times 10^{-5}-10^{-3}$ M, which strongly indicates that the microscopic structure of the aggregates does not change in this concentration range.

Cryo-electron Microscopy. A few microliters of aggregate suspension (5×10^{-4} M $TPPS_4$) were placed on a quantifoil 3.5/1 holey carbon-coated grid (Quantifoil micro tools GmbH, Jena, Germany). The grids were automatically blotted and vitrified using the vitrobot (FEI, Eindhoven, The Netherlands). Frozen hydrated specimens were investigated with a Gatan cryo-stage (Model 626, Gatan, Pleasanton, CA) in a Philips CM120 cryo-electron microscope (Philips, Eindhoven, The Netherlands) operating at 120 keV and in a Tecnai G2 Polara electron microscope (FEI, Eindhoven, The Netherlands) equipped with a Gatan energy filter. Images were recorded in the zero-loss imaging mode at 300 keV under low-dose conditions with a slow scan charge-coupled device (CCD) camera (Gatan, Pleasanton, CA).[32]

Absorption and Linear Dichroism Spectroscopy. Absorption spectroscopy of $TPPS_4$ aggregates was performed using a Lambda 900 UV/vis/NIR spectrometer (PerkinElmer). Orientation of the aggregates for the linear dichroism (LD) measurements was achieved by means of circulation of the solution through a 0.1 mm thick quartz flow-cell (Starna) at approximately 2 m/s velocity. Since at flow velocities above 30 cm/s, the LD signal amplitude reaches its saturation value and remains constant at flow velocities up to 2.5 m/s, we assume that in this velocity range nearly perfect alignment of the aggregates along the cell is maintained. In case of partial alignment, one would expect a noticeable LD signal dependence on the flow speed. Absorption spectra of oriented aggregates were measured both with light polarized parallel (A_{par}) and

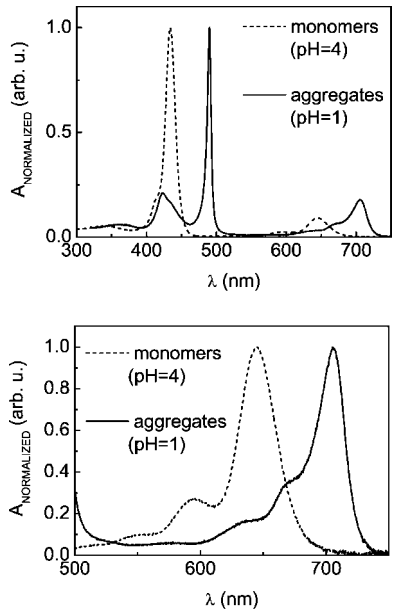

Figure 2. Normalized absorption spectra of various forms of $TPPS_4$ protonated monomers at pH = 4 (dashed line) and aggregates at pH = 1. Measurements were performed with 2×10^{-5} M $TPPS_4$ solutions. The lower panel shows a magnification of the Q band region in the upper panel.

perpendicular (A_{perp}) to the axes of the aggregates. The LD values are given by the difference of the two: LD = $A_{par} - A_{perp}$.

Isotropic absorption spectra were recorded in the same setup with unpolarized light and with no flow in the cell; a 2 mm quartz cell (Starna) was used for low concentration solutions. All spectroscopy experiments were performed at room temperature.

Experimental Results

The absorption spectrum of $TPPS_4$ monomers (protonated form at pH = 4) is shown by the dashed line in Figure 2. It shows a number of peaks: the B band at 434 nm, which originates from the degenerate B_x and B_y transitions, and a number of Q band related peaks at 505, 555, 595, and 645 nm, which originate from nondegenerate $Q_y(0-1)$, $Q_y(0-0)$, $Q_x(0-1)$, and $Q_x(0-0)$ transitions, respectively.[33] Here x and y refer to the orientations of the various electronic transition dipoles within the molecule; see Figure 1b. The lower panel of Figure 2 shows the Q band region in more detail.

Figure 2 also presents the absorption spectrum of the aggregated species (pH = 1, solid line). The same spectrum, together with the linear dichroism spectrum of the aggregates is shown in Figure 3. The signature of aggregate formation can be observed especially clearly in the vicinity of the B band, in particular through the appearance of the narrow red-shifted peak at 490 nm,[34,35] polarized parallel to the axis of the aggregate. The sharpness of this band is characteristic for J-aggregation. The other, somewhat less pronounced, B band related peak, polarized perpendicular to the axis of the aggregate, is located at 423 nm. The Q band region shows one polarized transition (parallel to the axis of the aggregates) at 709 nm, and a number of minor peaks around 670, 640, and 570 nm which show no significant polarization.

It should be noted that experiments at very low dye concentrations (below 10^{-7} M), for which the $TPPS_4$ molecules remain unaggregated, reveal that the $TPPS_4$ monomeric spectra remain virtually unchanged in a wide range of acidity (pH = −1−4).[36] This strongly suggests that the electronic structure of the monomers at pH = 1 is the same as at pH = 4 and implies that the shifts when changing from pH = 4 to 1 are really due to aggregation, i.e., due to excitonic interactions between the molecules.

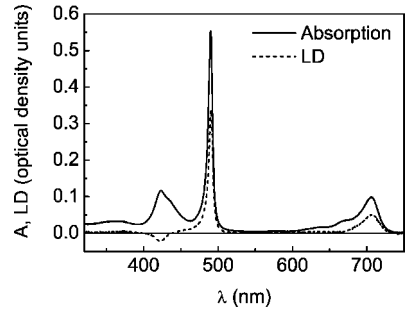

Figure 3. Absorption and LD spectra of 10^{-4} M pH 1 aqueous solution of $TPPS_4$ aggregates. Measurements were performed in a 0.1 mm cell.

The cryo-electron microscopy images displayed in Figure 4 clearly confirm the tubular structure of the $TPPS_4$ aggregates. In particular, the circular cross-section of the quasi-one-dimensional features is evident from the two short cylindrical fragments (indicated by arrows) that are oriented perpendicular to the plane of the image. The lengths of the tubules vary over a broad range and reach up to several micrometers. Their average diameter (distance between the centers of the walls) is 17.9 nm, though the diameters are not monodispersed in contrast to the data reported in ref 17. The wall thickness of the tubules is difficult to determine precisely because of the defocused mode of the microscope, but it does not exceed 2.5 nm. A detailed statistical analysis of the diameter distribution was not performed, since this distribution appears rather condition dependent: it is very narrow (on the order of the resolution −0.6 nm) when the aggregation proceeds in solutions of low concentration (10^{-5} M), while it is much broader (standard deviation 1.5 nm) when the aggregates are prepared from high-concentration solutions (10^{-3} M). The effect of aggregation rate on the structure of aggregates was not studied quantitatively, but, not surprisingly, slower aggregation leads to aggregates which correspond to the most energetically favorable structure. It is likely that other conditions, such as temperature or pH value, have some influence on the diameter distribution as well. In all observed cases, however, the average and the most probable diameter of the tubules remains 17.9 ± 0.5 nm. Given the fact that the radius of the cylindrical aggregates is much larger than the dimensions of a single $TPPS_4$ molecule, it is natural to assume that the molecular arrangement of the cylindrical aggregates locally does not deviate significantly from its planar counterpart and that the absorption and LD spectra are rather insensitive to the diameter variations.

Model

Our formalism is an extension of previous work by Knoester and co-workers on exciton models for cylindrical aggregates, which has been applied successfully to model the optical properties of tubular aggregates of carbocyanine molecules[12] and chlorosomes of green bacteria.[6,37] In this model, the molecular arrangement in the tubular structure is thought of as originating from a planar aggregate wrapped onto a cylindrical surface in a seamless way. A Frenkel exciton model, which accounts for the resonant dipole−dipole interactions between the various molecules in the aggregate, is then used to describe the relevant collective excited states.

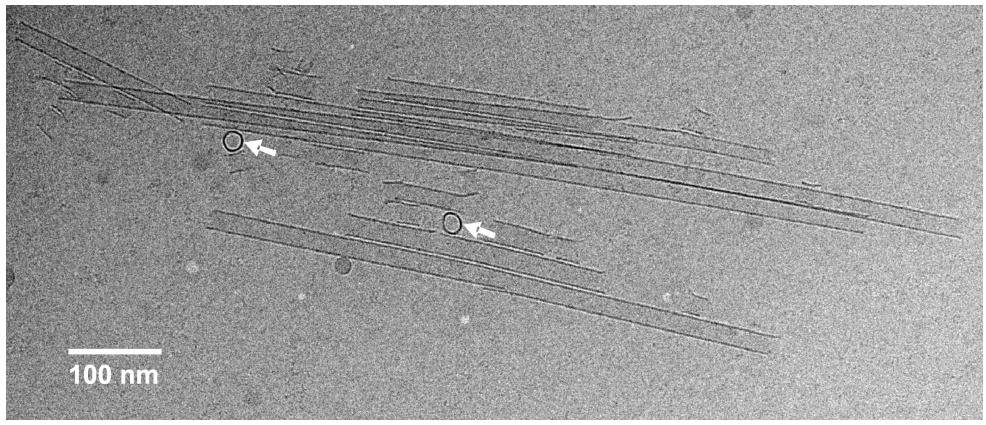

Figure 4. Cryo-EM image of $TPPS_4$ tubules. Two fragments of tubules oriented perpendicular to the plane of the image are visible (marked with arrows).

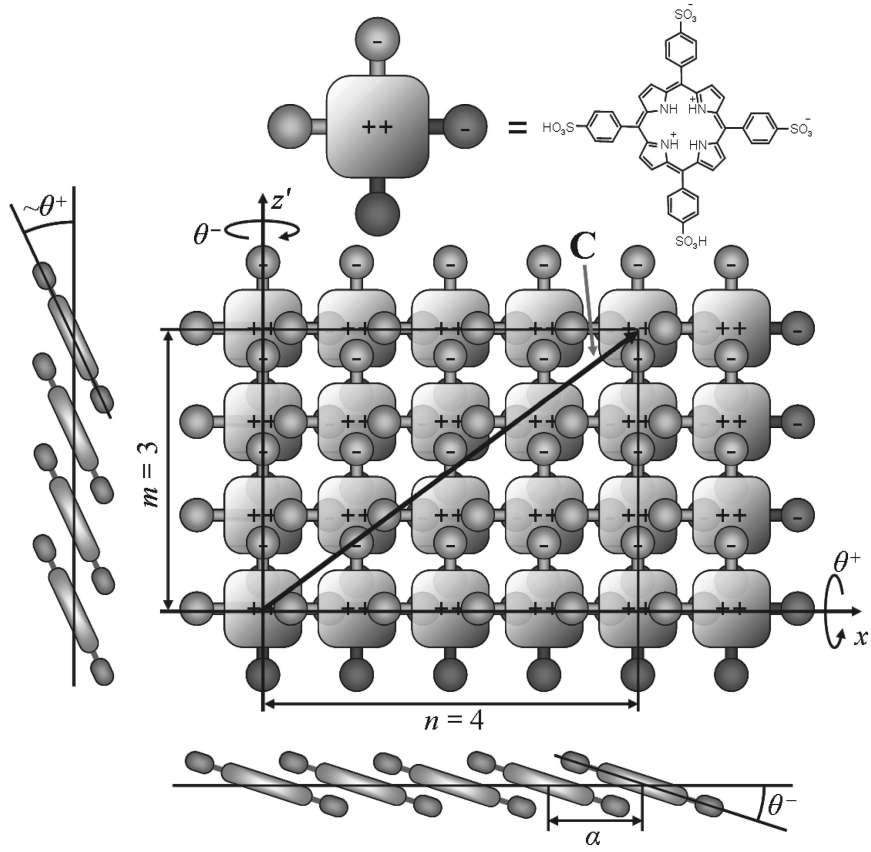

Figure 5. Planar geometry of the aggregate wall. The $TPPS_4$ monomers have been drawn schematically, with charged groups of the monomers indicated; see also Figure 1. The darker parts lie below the $x'z'$ plane, while the lighter parts lie above it. The square lattice and the perpendicular axes $\mathbf{x}'$ and $\mathbf{z}'$, in whose respective directions the lattice vectors $\mathbf{a}_1$ and $\mathbf{a}_2$ are oriented, have been drawn in the center. Also, an example of a chiral vector $\mathbf{C} = (n, m) = (4, 3)$ has been drawn, and to emphasize the tilted orientation of the monomers, the tilting angles θ^+ and θ^- over which each monomer should be rotated have been indicated as well. The lattice parameter a is of the order of 1 nm. The side views on the left and the bottom illustrate the tilted structure of these $TPPS_4$ monomers, with tilting angles θ^+ and θ^- in the order of 15−25°.

For an ordered long aggregate, the cylindrical symmetry restricts the optically allowed transitions from the ground-state to three superradiant contributions: one that is polarized along the axis of the cylinder and two that are degenerate and which are polarized perpendicular to this axis. The model thus predicts two main absorption bands with different LD signs, a feature that survives moderate disorder. The main extension which we apply to this model is that we account for four optical transitions per molecule, instead of just one. We allow for mixing of the B_x and the B_y transitions due to the intermolecular interactions, as well as mixing of the Q_x and the Q_y transitions. The incorporation of these different transitions also forces us to be more careful when generating the orientations of the molecular transitions dipoles within the cylinder. The latter will be done in the section The Cylindrical Geometry, while the Hamiltonian is introduced in the section Hamiltonian and Spectra. The calculation of the optical properties for long ordered aggregates is addressed in the section Ordered Aggregate and Optical Selection Rules, and the incorporation of disorder in this calculation is explained in the section Effects of Disorder.

Cylindrical Geometry. We generate the molecular organization by rolling a planar aggregate onto a cylindrical surface, a method that is justified by the fact that the cylinder radius is large compared to the molecule. We start from a square planar

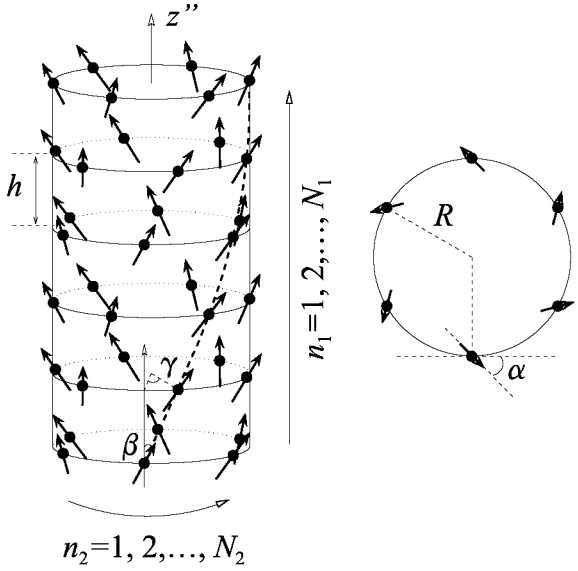

Figure 6. Cylindrical aggregate in the stack-of-rings representation with the angles α, β, and γ, as well as the cylinder radius R and the interring separation h indicated (taken from ref 6). Transition dipoles are displayed by arrows; for clarity, only one monomer transition has been considered here. To the right is shown a single ring with the projection of the dipoles on the plane of the ring.

lattice, with lattice vectors $\mathbf{a}_1 = a\hat{\mathbf{x}}'$ and $\mathbf{a}_2 = a\hat{\mathbf{z}}'$, as displayed in Figure 5. Each lattice point marks the center position of a $TPPS_4$ molecule; the molecules are tilted out of the plane, such that negatively charged SO_3^- groups lie above and below the positive nitrogen atoms. The symmetry of the molecule in its zwitterionic form suggests that indeed we deal with a square lattice. The primed coordinate system should not be confused with the molecular x and y axes, which, as indicated in Figure 1, are oriented along the lines between opposite nitrogen atoms. These molecular axes mark the directions of the molecular transition dipoles, which all lie in the plane of the porphyrin ring. Specifically, before tilting the B_x and Q_x transitions have dipoles that make an angle of $-45°$ with $\mathbf{a}_1$, while the B_y and Q_y transition dipoles make an angle of $+45°$ with $\mathbf{a}_1$.[33,38]

The tilting is described by rotating the molecular coordinate system with respect to the lattice coordinate system. This is done by first rotating each molecular coordinate system over an angle θ^+ around the x'-axis, or equivalently, around the vector $\hat{\mathbf{x}} + \hat{\mathbf{y}}$ in the molecular plane. Subsequently, we rotate the molecule over an angle θ^- around the vector $\hat{\mathbf{y}} - \hat{\mathbf{x}}$. Motivated by the symmetry of the porphyrin, we expect the tilt angles to have a comparable magnitude. The signs, corresponding to counterclockwise (positive) or clockwise (negative) rotations when looking toward the origin, are allowed to differ. The sequence of these rotations is described by a rotation matrix A given by

$$A = \begin{pmatrix} \cos\theta^- & \sin\theta^-\cos\theta^+ & \sin\theta^-\sin\theta^+ \\ -\sin\theta^- & \cos\theta^-\cos\theta^+ & \cos\theta^-\sin\theta^+ \\ 0 & -\sin\theta^+ & \cos\theta^+ \end{pmatrix} \quad (1)$$

Of course, the tilting will also rotate the molecular transition dipole vectors specified above.

The cylindrical configuration is obtained by rolling the above planar structure over the chiral vector $\mathbf{C}$, such that the end point of $\mathbf{C}$ coincides with its origin; see also Figure 5. The length of $\mathbf{C}$ is equal to the circumference of the cylinder, $|\mathbf{C}| = 2\pi R$. The axis of the cylinder is oriented perpendicularly to $\mathbf{C}$. The orientation of $\mathbf{C}$ is characterized by the so-called rolling angle θ it makes with the $\mathbf{x}'$-direction.

It has been shown in ref 6 that the cylindrical aggregate may always be regarded as a stack of N_1 rings (labeled n_1), each containing N_2 molecules (labeled n_2); each monomer is now denoted by $\mathbf{n} = (n_1, n_2)$ (see Figure 6). This representation is useful, because it allows one to exploit the cylindrical symmetry to determine optical selection rules.[6,39] In this representation, neighboring rings are separated by a distance h and rotated relative to each other over a helical angle γ. The rings are stacked in the direction of the cylinder's axis, oriented perpendicular to $\mathbf{C}$. We will refer to this as the z''-axis. The plane perpendicular to the axis is the $x''y''$-plane. Using geometrical arguments, it is straightforward to determine the parameters N_1, N_2, h, and γ from the original lattice structure and the vector $\mathbf{C}$; we refer to ref 6 for details. In addition, we introduce the label j to distinguish between different molecular transitions. Finally, it is useful to specify the orientation of each molecular transition dipole $\boldsymbol{\mu}_{\mathbf{n}j}$ by the angle β_j which it makes with the cylinder axis and the angle α_j between the projection of $\boldsymbol{\mu}_{\mathbf{n}j}$ on the ring plane and the local tangent of the ring. These angles, which do not depend on $\mathbf{n}$, can be found in a straightforward way from the three-dimensional orientation of the transition dipole moments after application of the tilting (operator A) and the orientation of $\mathbf{C}$ in the plane of the lattice.

Using the stack-of-rings representation and the notation introduced above, the position vector of the molecule at site $\mathbf{n} = (n_1, n_2)$ and the dipole moment of its jth transition are, within the $x''y''z''$ coordinate system, given by

$$\mathbf{r}_{\mathbf{n}} = (R\cos(n_2\phi_2 + n_1\gamma), R\sin(n_2\phi_2 + n_1\gamma), n_1 h) \quad (2)$$

$$\boldsymbol{\mu}_{\mathbf{n}j} = (-\mu_j \sin\beta_j \sin(n_2\phi_2 + n_1\gamma - \alpha_j), \mu_j \sin\beta_j \cos(n_2\phi_2 + n_1\gamma - \alpha_j), \mu_j \cos\beta_j) \quad (3)$$

with $\phi_2 = 2\pi/N_2$ and μ_j as the magnitude of the dipole of transition j. Note that this structure provides a generic description of a tiled, planar aggregate wrapped onto a cylindrical surface, as long we assume a configuration with one $TPPS_4$ molecule per unit cell. All such cylindrical geometries can be represented by an appropriate choice of the various parameters described above.

Hamiltonian and Spectra. The optically active electronic states of the $TPPS_4$ aggregates are modeled by a Frenkel exciton Hamiltonian, accounting for the fact that $TPPS_4$ has four transitions per molecule. Given the large energy separation between the optically relevant exciton states caused by the B and Q transitions, we will neglect their coupling and perform the calculations for these two bands separately. For systems where the optically active Q band exciton states occur much closer in energy to the B band exciton states, effects such as intensity borrowing and additional shifts may become important. We refer to refs 40−42 for the effects of mixing B and Q type transitions in two related systems, β-tetraethyl-tetrapyridinyl-porphyrin aggregates[40] and chlorophylls/bacteriochlorophylls.[41,42]

The Hamiltonian we use thus reads ($\hbar = 1$)

$$H = \sum_{\mathbf{n},j} \omega_{\mathbf{n}j} |\mathbf{n}j\rangle\langle\mathbf{n}j| + \sum'_{\mathbf{n},\mathbf{m},j,j'} J_{jj'}(\mathbf{n} - \mathbf{m}) |\mathbf{n}j\rangle\langle\mathbf{m}j'| \quad (4)$$

where $|\mathbf{n}j\rangle$ denotes the state of the aggregate in which transition j of molecule $\mathbf{n}$ has been excited, while all other molecules are

in their ground state. As we deal with the B and the Q transitions separately, we will from now on assume that the transition label j takes only two values ($j = x, y$), which distinguish between the x and y polarized transitions in both bands.

The first term in eq 4 accounts for the energy $\omega_{\mathbf{n}j}$ of the molecular transitions. In general, we will allow for energy disorder and choose random and uncorelated values for $\omega_{\mathbf{n}j}$ from a Gaussian distribution with a given standard deviation σ_j and mean value ω_j. In the case of the B band, the x and y transitions are degenerate, implying that $\omega_x = \omega_y$; for the Q band, this degeneracy is lifted[33] (also see Figure 2). The second term in eq 4 represents the interactions between the various molecular transitions. Here the prime on the summation excludes the term with $\mathbf{n} = \mathbf{m}$. Because the distances between nearest-neighbor molecules are similar ($\sim$0.5 nm)[38,43] to their dimensions,[44] we cannot use a point-dipole approximation for these interactions. Rather, we model them as interactions between the extended dipoles associated with the molecular transitions. Thus, we model each dipole as two point charges (q and $-q$) separated by a distance L, such that the corresponding transition dipole moment qL has the correct magnitude, orientation, and position. The interaction between two transition dipole moments is then given by the Coulomb interaction between the four charges (see, e.g., ref 12).

For a particular realization of the disorder, the (exciton) eigenstates of eq 4 may be written $|\mathbf{q}\rangle = \sum_{\mathbf{n}j} \varphi_{\mathbf{q}\mathbf{n}j}|\mathbf{n}j\rangle$, where $\varphi_{\mathbf{q}\mathbf{n}j}$ denotes the $(\mathbf{n}j)$th component of eigenvector referred to by the quantum label $\mathbf{q}$; the corresponding eigenvalue gives the energy $E_{\mathbf{q}}$ of this eigenstate. In terms of these quantities, the isotropic absorption spectrum reads

$$A(\omega) = \langle\langle \sum_{\mathbf{q}} O_{\mathbf{q}} \delta(\omega - E_{\mathbf{q}})\rangle\rangle \tag{5}$$

with the oscillator strengths

$$O_{\mathbf{q}} = \langle |\sum_{\mathbf{n},j} \varphi_{\mathbf{q}\mathbf{n}j}\mu_{\mathbf{n}j}\cdot\mathbf{e}|^2\rangle = \sum_{\mathbf{n},j,\mathbf{m},j'} \varphi_{\mathbf{q}\mathbf{n}j}\varphi^*_{\mathbf{q}\mathbf{m}j'}O_{\mathbf{n}j\mathbf{m}j'} \tag{6}$$

where the coefficients $O_{\mathbf{n}j\mathbf{m}j'}$ are given by

$$O_{\mathbf{n}j\mathbf{m}j'} = \langle(\mu_{\mathbf{n}j}\cdot\mathbf{e})(\mu_{\mathbf{m}j'}\cdot\mathbf{e})\rangle \tag{7}$$

The double angular brackets $\langle\langle\cdots\rangle\rangle$ in eq 5 indicate an average over the disorder realizations, while the single angular brackets $\langle\cdots\rangle$ in eqs 6 and 7 signify an orientational average over the orientations of the cylinder relative to the polarization vector $\mathbf{e}$ of the incoming linearly polarized light.

The linear dichroism is taken in a sample where all cylinders are oriented along their symmetry axis and is defined as the difference in absorption between light polarized parallel and perpendicular to this axis. It is given by

$$\mathrm{LD}(\omega) = \langle\langle \sum_{\mathbf{q}} \mathrm{LD}_{\mathbf{q}} \delta(\omega - E_{\mathbf{q}})\rangle\rangle \tag{8}$$

with

$$\mathrm{LD}_{\mathbf{q}} = \sum_{\mathbf{n},j,\mathbf{m},j'} \varphi_{\mathbf{q}\mathbf{n}j}\varphi^*_{\mathbf{q}\mathbf{m}j'}\mathrm{LD}_{\mathbf{n}j\mathbf{m}j'} \tag{9}$$

where the coefficients $\mathrm{LD}_{\mathbf{n}j\mathbf{m}j'}$ are given by

$$\mathrm{LD}_{\mathbf{n}j\mathbf{m}j'} = (\mu_{\mathbf{n}j}\cdot\mathbf{z}'')(\mu_{\mathbf{m}j'}\cdot\mathbf{z}'') - \langle(\mu_{\mathbf{n}j}\cdot\mathbf{e}_\perp)(\mu_{\mathbf{m}j'}\cdot\mathbf{e}_\perp)\rangle \tag{10}$$

The double angular brackets $\langle\langle\cdots\rangle\rangle$ in eq 8 again imply an average over disorder realizations, while $\langle\cdots\rangle$ in eq 10 denote an average over rotations of the cylinder around its axis, relative to the polarization vector $\mathbf{e}_\perp$ of the light in the $x''y''$-plane.

Due to the simple cylindrical geometry, it is possible to derive the orientational averages introduced above analytically; the resulting expressions for $O_{\mathbf{n}j\mathbf{m}j'}$ and $\mathrm{LD}_{\mathbf{n}j\mathbf{m}j'}$ are given in the Appendix.

Ordered Aggregate and Optical Selection Rules. It is useful to consider the case without disorder. Then, the cylindrical symmetry dictates Bloch character for the exciton wave functions in the n_2 direction. If we assume that the cylinders are long, we may also impose Bloch wave functions in the n_1 direction. We thus introduce states of the form $|\mathbf{k}j\rangle = |(k_1, k_2)j\rangle = N^{-1/2}\sum_{n_1,n_2} \exp[-i(k_1\phi_1 n_1 + k_2\phi_2 n_2)]|\mathbf{n}j\rangle$, with $\phi_i = 2\pi/N_i$, $k_i = 0, \pm1,..., \pm(N_i/2 - 1), N_i/2$ for N_i even,[45] and $N = N_1N_2$. Due to the fact that we deal with two coupled molecular transitions (either in the B band or in the Q band), these new states do not fully diagonalize the Hamiltonian. Similar to the situation with two molecules per unit cell,[46] the problem is reduced to a 2×2 problem for every wave vector $\mathbf{k}$. The matrix that still needs to be diagonalized for a given $\mathbf{k}$ reads

$$H(\mathbf{k}) = \begin{pmatrix} \omega_x + J_{xx}(\mathbf{k}) & J_{xy}(\mathbf{k}) \\ J_{yx}(\mathbf{k}) & \omega_y + J_{yy}(\mathbf{k}) \end{pmatrix} \tag{11}$$

with $J_{jj'}(\mathbf{k}) = \sum'_{\mathbf{n}} J_{jj'}(\mathbf{n}) \exp[-i(k_1\phi_1 n_1 + k_2\phi_2 n_2)]$, where the summation should be taken consistent with the periodic boundary conditions. The eigenvalues of this matrix are denoted $E_{\mathbf{k}l}$ and represent the energies of the two eigenstates with wave vector $\mathbf{k}$, distinguished by the branch label $l = 1, 2$. The corresponding eigenvectors are denoted $\tilde{\varphi}_{lj}(\mathbf{k})$. With this notation, the total eigenvectors introduced in the section Hamiltonian and spectra take the form

$$\varphi_{\mathbf{k}l\mathbf{n}j} = \frac{1}{\sqrt{N}} e^{-i(k_1\phi_1 n_1 + k_2\phi_2 n_2)}\tilde{\varphi}_{lj}(\mathbf{k}) \tag{12}$$

where the general quantum label $\mathbf{q}$ has been replaced by the composite label $\mathbf{k}l$. We note that generally the splitting within the "Davydov" doublets is not only due to the interaction $J_{xy}(\mathbf{k}) = J_{yx}(\mathbf{k})^*$ between the two underlying transitions, but also because $J_{xx}(\mathbf{k})$ and $J_{yy}(\mathbf{k})$ may differ considerably, due to the fact that the two relevant transition dipole moments are oriented differently relative to the intermolecular separations.

For the ordered aggregate, the absorption and linear dichroism spectra take the generic form

$$S(\omega) = -\frac{1}{\pi}\mathcal{I}\sum_{\mathbf{k}l} X_{\mathbf{k}l}\frac{1}{\omega - E_{\mathbf{k}l} + i\eta} \tag{13}$$

Here, $\mathcal{I}$ denotes taking the imaginary part, η is introduced to account for homogeneous broadening, and $X_{\mathbf{k}l}$ equals the oscillator strength $O_{\mathbf{k}l}$ or the dichroism strength $\mathrm{LD}_{\mathbf{k}l}$ for the absorption and LD spectrum, respectively, which are obtained from eqs 6 and 9. Due to the Bloch nature of the eigenfunctions, it is possible to further evaluate the latter expressions. The results

are direct extensions of earlier results where only one transition per molecule was considered.[6,39,47] Specifically, we find two peaks in the spectrum associated with the Davydov split states with $\mathbf{k} = \mathbf{0}$; these peaks correspond to transitions that are polarized parallel to the cylinder axis and thus yield a positive LD signal. We also find two peaks due to the transitions with $\mathbf{k} = \pm\mathbf{k}_h$, where $\mathbf{k}_h = (\gamma/\phi_1, 1)$, the helical wave vector (in the case of incommensurate parameters, k_1 is replaced by the integer closest to γ/ϕ_1).[6] Due to the fact that we have two transitions per molecule, this involves in total four transitions, which are all polarized perpendicular to the cylinder axis and thus contribute negative peaks to the LD spectrum. Because the energy does not depend on the sign of the wave vector, these four transitions only contribute two peaks to the absorption and the LD spectrum. We thus find in total four peaks in the absorption spectrum, two with positive LD and two with negative LD.[48]

The areas of these peaks are given in the Appendix; characteristic for the superradiant nature of the underlying states, they all scale proportionally to N, the number of molecules in the cylinder. However, the ratios of the peak areas within and between Davydov doublets may vary strongly with system parameters, in particular with the rolling and tilting angles. The same is true for the energy separations between the peaks. As a consequence, under certain circumstances not all of the above predicted peaks may be visible in the spectrum, either because energies are too close or because the area of a particular peak becomes too small. An illustration will be given at the end of the next subsection. As we will see later, these dependencies are responsible for the fact that in the B band region of $TPPS_4$ aggregates only two and not four major peaks are discerned.

Effects of Disorder. Effects of disorder in molecular aggregates are often investigated using numerical simulations.[49,50] While in principle this offers a straightforward technique, the number of molecules in $TPPS_4$ aggregates of even moderate lengths is too large (around 65 molecules per nm of length) to make this a viable option. However, it is well-known[37,51] that linear optical spectra of disordered molecular aggregates may be calculated with high accuracy using the coherent potential approximation (CPA).[52−54] In the CPA the disordered system is replaced by an effective ordered system in which a complex self-energy $\Sigma(\omega)$ is added to every transition energy. Thus, the resulting spectra take the same form as eq 13, except that the denominator $\omega - E_{\mathbf{k}l} + i\eta$ is replaced by $\omega - E_{\mathbf{k}l} - \Sigma(\omega) + i\eta$.

The self-energy $\Sigma(\omega)$ follows from the self-consistency condition

$$\left\langle \frac{\omega_{\mathbf{n}j} - \Sigma(\omega)}{1 - (\omega_{\mathbf{n}j} - \Sigma(\omega))\langle \hat{G}(\omega)\rangle_{\mathbf{nn}jj}} \right\rangle = 0 \qquad (14)$$

where the averaging is performed over the distribution of the site energy $\omega_{\mathbf{n}j}$ and the site diagonal matrix element of the averaged Green's function is given by

$$\langle \hat{G}(\omega)\rangle_{\mathbf{nn}jj} = \sum_{\mathbf{k}l} \frac{|\varphi_{\mathbf{k}l\mathbf{n}j}|^2}{\omega - E_{\mathbf{k}l} - \Sigma(\omega) + i\eta} \qquad (15)$$

The self-energy can be obtained numerically from eq 14 by an iterative procedure.[37,51] Once the self-energy $\Sigma(\omega)$ has been calculated,[55] the spectra follow directly from eq 13 with the denominator replacement mentioned above and the oscillator and dichroism strength given in the Appendix.

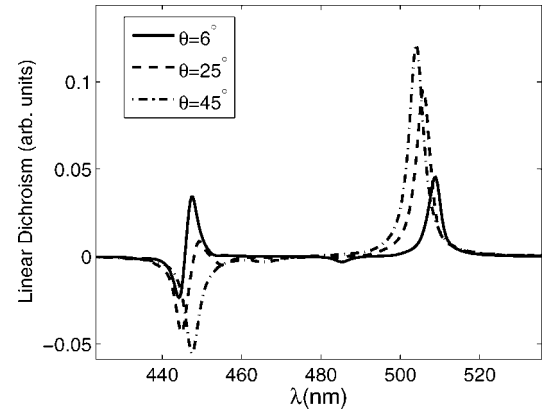

Figure 7. Calculated dichroism spectra for three different rolling angles indicated in the panel. Narrow peak widths, corresponding to $\eta = 100$ cm^{-1} and Gaussian disorder with a standard deviation of $\sigma = 60$ cm^{-1} (accounted for using the CPA), have been chosen so that the doublet structure is clearly visible in the low-wavelength doublet. In the high-wavelength doublet, the peaks are too close to distinguish the two peaks, and the linear dichroism signal is the sum of a positive and negative contribution. The peaks have been obtained for point dipole interactions, a lattice constant of $a = 1$ nm, and tilting angles $\theta^+ = -\theta^- = 25°$; the qualitative behavior is identical for extended dipoles and different choices of a, θ^+, and θ^- within reasonable bounds.

To illustrate typical results, in Figure 7 we show the LD spectrum in the B band region obtained by using the CPA for three different rolling angles θ, taking the homogeneous width $\eta = 100$ cm^{-1}, the disorder width $\sigma = 60$ cm^{-1}, and using tilting angles of equal magnitude and opposite sign, $\theta^+ = -\theta^- = 25°$. All other parameters are chosen identical to the ones that we will find in the section Comparison to Experiment as the parameters that apply to the $TPPS_4$ aggregates; the linewidths have deliberately been chosen rather small in order to give more insight into the details of the spectrum. Clearly, even the qualitative shape of the spectrum depends on the rolling angle, as was already anticipated in the section Ordered Aggregate and Optical Selection Rules. For a rolling angle of $\theta = 6°$, we can clearly distinguish three of the four peaks predicted in the section Ordered Aggregate and Optical Selection Rules, in addition to a small secondary peak with a negative LD signal.[48] They originate from transitions to two pairs of states, one of each pair having a positive LD signal and the other one having a negative LD. The two peaks at around 500 nm coincide to a large degree, leading to a considerable cancelation of the LD signal and producing the small, positive LD peak shown in Figure 7. If the rolling angle is increased to $\theta = 25°$, we observe that for the upper pair (in wavelength) the positive LD contribution has increased while the negative LD contribution has decreased and vice versa for the lower pair. For the upper pair, this is reflected in the increased area, while for the lower pair this can be observed directly as the two contributions are more separated in energy. Finally, for $\theta = 45°$, the positive peak in the lower-energy pair has also disappeared, leaving us with a spectrum with just one positive and one negative peak. Such a spectrum resembles the spectrum of a cylindrical aggregate with just one transition per molecule, but, for realistic parameters, the energy splitting between both peaks is too large to be explained within that model. For tilting angles of different magnitude, $|\theta^+| \neq |\theta^-|$, a similar dependence of the peak structure on the rolling angle θ is observed, although in general the two-peak structure will occur for a different value of θ.

Comparison to Experiment

Parameters. Our model contains many parameters; in order to make a fit procedure meaningful, the values for as many of those as possible should be determined a priori, or at least constraints on their values should be determined. We start with the geometric parameters. Of those, the cylinder radius is best known, as it is directly observed in our cryo-EM experiments. We will take it as $R = 9$ nm, which is consistent with earlier sources.[16,17] The discrete nature of the lattice can produce small deviations in this radius, but these are well within the experimental error. Moreover, the large radius (as compared to the molecular size) implies that the molecular arrangement on the cylindrical surface is locally almost flat, which is reflected in the insensitivity of the simulated spectra to deviations in the cylinder radius. Through the relation $|\mathbf{C}| = 2\pi R$, the cylinder radius also fixes the length of the chiral vector $\mathbf{C}$; however, the rolling angle θ between $\mathbf{C}$ and the lattice vector $\mathbf{a}_1$ is not known and will be treated as a free parameter.

From small-angle X-ray scattering and molecular modeling, it is found that the lattice constant $a \approx 1$ nm,[38,43] which we take as an initial value in our model. As we will see in the Results section, the comparison between theory and experiment adjusts this value to some extent. The final geometric parameters are the tilt angles θ^+ and θ^- introduced in the section Cylindrical Geometry. These angles have been estimated to be in the region of $\pm 15-25°$.[25,26,38,43,56] Hence, their values will also be used as (almost) free parameters.

We now turn to parameters characterizing the molecular transitions and interactions. The mean energy of the monomeric B_x and B_y transitions are taken to be $\omega_x = \omega_y = 23\,041$ cm^{-1}, in agreement with the experimental monomer peak at $\lambda = 434$ nm. These degenerate transitions have perpendicular transition dipole moments, whose orientations have been specified in the section Cylindrical Geometry already. The magnitude of these dipoles, as estimated from the spectroscopical data in ref 57, is $\mu = 11.3$ D, a value comparable to typical transition dipole moments in other porphyrins. Our experiments reveal a similar magnitude of μ, but because of the more accurate concentration calibration procedure employed in ref 57, we will further rely on the value estimated from the literature data. When using the extended dipole representation, it is assumed that the charges q and $-q$ are separated by a distance of $L = 0.5$ nm, corresponding to an approximate diameter of the porphyrin ring. The charge q is taken as $q = 0.48e$ to reproduce the correct monomer transition dipole moment.

The rich structure of the Q band monomer transitions and the importance of vibrational coupling[21,26,33] makes the modeling of the associated aggregate bands a more complicated matter. Four Q-related peaks can be observed in the Q band region of the monomer (cf. also Figure 2); their frequencies and assignments have been given in the section Experimental Results. The degeneracy of x and y transitions is lifted due to distortion of the monomer.[33] Strictly speaking, a correct treatment of the Q band should include the vibrations responsible for this distortion and for the vibrational side bands in the monomer spectrum. As this would considerably complicate our analysis, we will ignore these vibrational effects and use monomeric transition frequencies that agree with the peak positions of the $Q_x(0-0)$ and $Q_y(0-0)$ transitions, namely $\omega_x = 15\,504$ cm^{-1} and $\omega_y = 18\,182$ cm^{-1}. The magnitude of the transition dipole moments, relative to those corresponding to the B band, can be obtained from experiment by comparing the integrated absorbances for the peaks in the monomer spectrum. Using $\mu = 11.3$ D for both B band transitions, this gives $\mu_x = 7.4$ D and $\mu_y = 2.3$ D for the Q band. The orientations of these dipole moments are assumed to be parallel to those for the monomeric B transitions. Finally, also for the Q band dipoles, we assume a charge separation of $L = 0.5$ nm.

The final model parameters to be determined are the homogeneous linewidths η and the disorder values σ. We will assume that the disorder does not differ significantly for the two polarizations within each band. This leaves us with two values for σ to be determined, one for the B and one for the Q transitions; their magnitudes are considered free parameters, fixed such that the simulated aggregate peaks obtain the correct widths. To this end, we should first determine the homogeneous linewidths for the various exciton transitions. While in reality, these widths are energy dependent and should be modeled in a microscopic way,[58,59] we use a phenomenological approach by assuming them to be constant within each one of the dominant exciton peaks observed in the spectrum.

We start from the strong B peak at 490 nm. From fluorescence measurements which we carried out, the lifetime of the 490 nm peak can be estimated to be smaller than or of the order of the resolution of the apparatus, i.e., $\tau \approx 150$ fs, which corresponds to $\eta \approx 100$ cm^{-1}. This short lifetime is probably mostly due to relaxation into the Q band excitons. The thus obtained value for η, or a somewhat larger one corresponding to a shorter lifetime, is not sufficient to fully account for the line width of the peak 490 nm; the remainder is due to the static energy disorder. This suffices to determine the value for σ, given that values have been chosen for the free geometric parameters (in particular the rolling angle and the tilt angles). We have found that for the optimal values of these angles, we should take $\sigma = 400$ cm^{-1} to reproduce a peak at 490 nm of the appropriate line width (see the Results section). Using the same σ value for the 423 nm peak and comparing to experiment reveals that this peak is dominated by homogeneous broadening, requiring $\eta = 600$ cm^{-1}, which corresponds to an ultrashort lifetime of $\tau \approx 30$ fs. This short lifetime is caused by relaxation inside the B band.

The same procedure is followed for the Q band. The Q band peak at 709 nm is the lowest-energy exciton state and is reported to have a rather long lifetime of over 50 ps.[25,60] Thus, its width is determined largely by disorder and not by lifetime broadening. We therefore set $\eta = 0$ cm^{-1} for this peak. For the optimal values of the rolling and tilt angles (vide infra), it then turns out that $\sigma = 720$ cm^{-1} is needed to reproduce the width and the low energy tail of this peak The much weaker second Q band obtained in the model calculations occurs at higher energies and is expected to have a much larger homogeneous broadening due to relaxation within the Q band. We use a reasonable estimate of the resulting lifetime of several tens of femtoseconds, or $\eta = 500$ cm^{-1}. We note that because this high-energy Q band is both weak and broad it is very hard to discern it in the spectrum and to determine its broadening parameters with reasonable precision.

Results

Using the approach described in the previous subsection, the really free parameters are θ, θ^+, θ^-, and the σ values for the B and the Q bands. The latter are easy to determine for any given choice of the unknown angles, by fitting the linewidths in the aggregate spectrum. This leaves us mainly with the three angles as important unknowns, which we vary over the entire parameter space.

The analysis of our simulations reveals that the relative signs of θ^+ and θ^- are dictated by the polarizations of the main peaks

in the bands. In order to reproduce the order of peak polarizations observed in experiment, θ^+ and θ^- should have opposite signs. The magnitudes of the tilting angles turn out to be important in fixing the positions of the peaks, while it also influences the areas of the peaks. The splitting between the two doublets (which are both observed as singlets) in the B band increases with increasing tilting angles, although an increase in the magnitude of one tilting angle can be partially compensated by reducing the magnitude of the other. In particular, we require that neither of the tilting angle magnitudes is larger than 30−35° to reproduce realistic splittings. Furthermore, in order to obtain a Q band peak of a sufficiently large area, our simulations suggest that the magnitudes of θ^+ and θ^- should be approximately equal.

Evaluating the oscillator strengths and the dichroism strengths given in the Appendix, it turns out that the rolling angle θ is crucial in determining the relative strengths of the peaks within the doublets with a positive and a negative LD transition. This was illustrated already in Figure 7 and discussed in the section Effects of Disorder. Because the experimental spectra do not show such doublets, we require a rolling angle that produces only one dominant peak per doublet for both, the B and the Q bands. For equal magnitudes of the tilting angles θ^+ and θ^-, this narrows down the range for θ to a small region around 45°. However, the large observed widths of the peaks may obscure a possible 2-fold origin of a peak in the absorption spectrum, as long as one of the two peaks in the doublet is sufficiently stronger than its companion. For the peak widths and intradoublet separations that are typical for our parameters in both bands, this is the case for rolling angles between 30° and 60°, or equivalently, a chiral vector which is oriented mostly in the direction of the weak Q_y transition.

The above findings guide the fitting procedure. In the end, we find that the parameters that yield the best simultaneous fit of the B and the Q band regions of the spectrum are $\theta = 45°$ and $\theta^+ = -\theta^- = 25°$. The η and σ values for this choice of the three angles were given in the previous subsection already. The splitting in the B band is rather sensitive to deviations from these tilting angles, which fixes their values within a couple of degrees for the parameters we use. The Q band is less sensitive to variations in the tilting angles, as these mostly cause shifts in the unimportant high-energy peak. Note that the values which we have found for the tilting angles fall within the range ±(15−25°) suggested by previous authors[25,26,38,43,56] but narrow down the uncertainty considerably. Translated into the cylindrical coordinate system, these parameters correspond to a cylinder with $N_2 = 43$, $a = 0.93$ nm (see below), $h = 0.66$ nm, and $\gamma = 4.2°$ while the dipole angles of the x- and y-oriented transitions are $\alpha_x = 17.4°$ and $\beta_x = 174.6°$ and $\alpha_y = 34.9°$ and $\beta_y = 84.9°$.

For the B and the Q band regions of the spectrum, the best simultaneous fits are plotted together with the experimental spectra in Figures 8 and 9, respectively. Indeed, a good agreement with experiment is observed. The deviation that stands out most is the fact that the simulation does not reproduce the shoulder in the Q band at $\lambda = 670$ nm. As mentioned above, vibrational interactions are important in the monomeric Q band. It may well be that the observed shoulder is, in fact, a vibrational sideband of the main exciton peak at $\lambda = 709$ nm; such side bands are not included in our model. Another deviation is that the asymmetry that is typical of J-bands is, surprisingly, not as pronounced in our simulations as it is in the experiments.

As mentioned in the section Parameters, the initial value for the lattice parameter a has been taken as $a = 1$ nm but was not known precisely. The fitting procedure suggests that

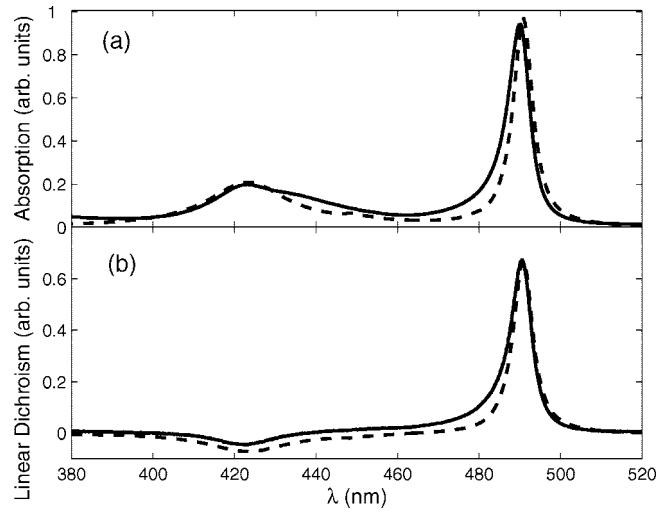

Figure 8. Comparison of the experimental (solid) and calculated (dashed) spectra for the B (Soret) band. Panel a shows the isotropic absorption spectra, while panel b features the linear dichroism spectra. Calculations were performed for Gaussian disorder with a standard deviation of $\sigma = 400$ cm^{-1}, a homogeneous broadening linewidth of $\eta = 600$ cm^{-1} and 100 cm^{-1} for the 423 and 490 nm peaks, respectively, a rolling angle of $\theta = 45°$, and tilting angles $\theta^+ = -\theta^- = 25°$. For the remaining parameters, see the text.

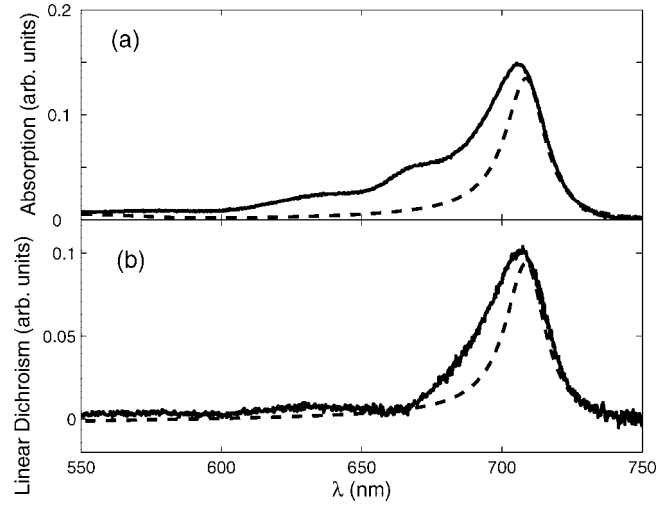

Figure 9. Comparison of the experimental (solid) and calculated (dashed) spectra for the Q-band region. Panel a shows the isotropic absorption spectra, while panel b features the linear dichroism spectra. Calculations were performed for Gaussian disorder with a standard deviation of $\sigma = 720$ cm^{-1}, homogeneous linewidths of $\eta = 500$ cm^{-1} and 0 cm^{-1} for the 550 (barely visible) and 709 nm peaks, respectively. All other parameters as in Figure 8.

$a = 0.93$ nm. Variations in a translate into variations in interaction strengths, with a smaller (larger) a leading to stronger (weaker) interactions $J_{jj'}(\mathbf{k})$. Since dipole−dipole interactions vary as $1/a^3$, a reduction of a by, for example, 10% increases the interactions by a factor of 1.4. Reproducing the experimental peak positions would then require a different set of fitting parameters; for the above example, the rolling angle θ would remain unchanged, the charge separation in the extended dipoles would increase to $L = 0.65$ nm, and the tilting angles would decrease to around $\theta^+ = -\theta^- = 23°$. In this manner, smaller or larger values of the lattice parameter a eventually necessitate unfeasibly large or small charge separation distances L. Therefore, the comparison between theory and experiment narrows down the possible error in the value of a to less than 10%.

Conclusions

In this paper, we studied the polarization dependent optical response of self-assembled aggregates of $TPPS_4$ molecules experimentally as well as theoretically. These aggregates have a tubular shape with a radius of 9 nm and a length of up to several micrometers, as observed in cryo-EM experiments reported here. We have shown that a Frenkel exciton model that accounts for four transitions per molecule (B_x, B_y, Q_x, and Q_y) yields good fits to the optical spectra over the entire visible range. Assuming a cylindrical structure with one $TPPS_4$ molecule per unit cell, the comparison between theory and experiment allowed us to propose a detailed molecular organization within the nanotube. In particular, this includes the rolling angle, which characterizes in what lattice direction a two-dimensional lattice should be rolled to obtain the nanotube, and the tilting angles, which determine how, prior to rolling, the molecules are tilted out of the plane of this two-dimensional lattice. Our results yield an error bar of a few degrees for these angles; variations in these angles correlate with parameters such as the lattice constant and the length of the extended transitions dipoles, both of which are known with an accuracy of the order of 0.1 nm.

It is interesting to see that the optical properties of such intriguing nanostructures with complicated electronic structure of the individual molecules can be explained quantitatively using a fairly simple phenomenological model. It also is of interest that the study of the optical properties yields more insight into the microscopic structure of such nanosystems.

In spite of the progress reported here, it would be worthwhile to extend the model, in particular to account for exciton−vibration coupling. As argued, the omission of such coupling may be the reason that our simulations do not reproduce the observed high-energy shoulder on the strongest Q band peak. This shoulder may be a vibrational sideband, which we can only properly account for by including a strong coupling between the excitons and a vibration.[61] In addition, the weaker coupling to other vibrations also deserves attention, as it is responsible for the relaxation within and between the various exciton bands. Including this relaxation allows one to go beyond the simple picture of an energy independent homogeneous line width and to study temperature dependence.[58]

Future work on this system should concentrate on dynamic properties, such as relaxation and energy transport. It would be particularly interesting to investigate whether excitation energy transport can occur over a sizable part of the length of the tube and to what extent exciton coherence plays a role in this. Multidimensional ultrafast spectroscopy on ensembles[62] as well as single-molecule spectroscopy with tip-enhanced excitation[63,64] provide promising tools to study these issues.

Acknowledgment. We thank Prof. D. A. Wiersma, Dr. A. Pugžlys, and Dr. C. Didraga for helpful discussions.

Appendix: Expressions for the Absorption Spectra

Straightforward calculation of the orientational averages in eqs 7 and 10 yields

$$O_{\mathbf{n}j\mathbf{m}j'} = \frac{1}{3}\mu_j\mu_{j'}(\cos\beta_j\cos\beta_{j'} + \cos[(n_2 - m_2)\phi_2 + (n_1 - m_1)\gamma]\sin\beta_j\sin\beta_{j'}\cos(\alpha_j - \alpha_{j'})) \quad (16)$$

and

$$\mathrm{LD}_{\mathbf{n}j\mathbf{m}j'} = \mu_j\mu_{j'}\left(\cos\beta_j\cos\beta_{j'} - \frac{1}{2}\cos[(n_2 - m_2)\phi_2 + (n_1 - m_1)\gamma]\sin\beta_j\sin\beta_{j'}\cos(\alpha_j - \alpha_{j'})\right) \quad (17)$$

For the special case of the homogeneous cylinder (and also in the case of disorder within the CPA), combining these expressions with the Bloch character of the wave functions, eq 12, leads to strong selection rules for the oscillator strengths $O_{\mathbf{q}} = O_{\mathbf{k}l}$ and the dichroism strengths $L_{\mathbf{q}} = L_{\mathbf{k}l}$. In analogy to ref 6, where only one transition per molecule was considered, we obtain in the limit of long cylinders

$$O_{\mathbf{k}l} = \sum_{j,j'}\frac{N\mu_j\mu_{j'}}{3}\tilde{\varphi}_{lj}(\mathbf{k})\tilde{\varphi}^*_{lj'}(\mathbf{k})\cos\beta_j\cos\beta_{j'}\delta_{\mathbf{k},0} + \sum_{j,j'}\frac{N\mu_j\mu_{j'}}{6}\tilde{\varphi}_{lj}(\mathbf{k})\tilde{\varphi}^*_{lj'}(\mathbf{k})\sin\beta_j\sin\beta_{j'}\cos(\alpha_j - \alpha_{j'})(\delta_{\mathbf{k},\mathbf{k}_h} + \delta_{\mathbf{k},-\mathbf{k}_h}) \quad (18)$$

where $\mathbf{k}_h = (k_1 = \gamma/\phi_1, k_2 = 1)$ denotes the helical wavevector. Analogously,

$$\mathrm{LD}_{\mathbf{k}l} = \sum_{j,j'}N\mu_j\mu_{j'}\tilde{\varphi}_{lj}(\mathbf{k})\tilde{\varphi}^*_{lj'}(\mathbf{k})\cos\beta_j\cos\beta_{j'}\delta_{\mathbf{k},0} - \sum_{j,j'}\frac{N\mu_j\mu_{j'}}{4}\tilde{\varphi}_{lj}(\mathbf{k})\tilde{\varphi}^*_{lj'}(\mathbf{k})\sin\beta_j\sin\beta_{j'}\cos(\alpha_j - \alpha_{j'})(\delta_{\mathbf{k},\mathbf{k}_h} + \delta_{\mathbf{k},-\mathbf{k}_h}) \quad (19)$$

Due to the symmetry of the energy with respect to the sign of $\mathbf{k}$, the above selection rules generate four peaks, two with positive LD and two with negative LD. The areas of the absorption peaks are

$$A_{0l} = \sum_{j,j'}\frac{N\mu_j\mu_{j'}}{3}\tilde{\varphi}_{lj}(\mathbf{k})\tilde{\varphi}^*_{lj'}(\mathbf{k})\cos\beta_j\cos\beta_{j'} \quad (20)$$

for the two peaks corresponding to transitions to the zero momentum states $\mathbf{k} = \mathbf{0}$, and

$$A_{hl} = \sum_{j,j'}\frac{N\mu_j\mu_{j'}}{3}\tilde{\varphi}_{lj}(\mathbf{k})\tilde{\varphi}^*_{lj'}(\mathbf{k})\sin\beta_j\sin\beta_{j'}\cos(\alpha_j - \alpha_{j'}) \quad (21)$$

for the two peaks corresponding to transitions to the helical states $\mathbf{k} = \pm\mathbf{k}_h$, while their LD areas are $\mathrm{LD}_{0l} = 3A_{0l}$ and $\mathrm{LD}_{hl} = -{}^3/_2A_{hl}$, respectively.

References and Notes

(1) Van Amerongen, H.; Valkunas, L.; van Grondelle, R. *Photosynthetic Excitons*; World Scientific: Singapore, 2000.

(2) McDermott, G.; Prince, S. M.; Freer, A. A.; Hawthornthwaite-Lawless, A. M.; Papiz, M. Z.; Cogdell, R. J.; Isaacs, N. W. *Nature* **1995**, *374*, 517.

(3) Staehelin, L. A.; Golecki, J. R.; Drews, G. *Biochim. Biophys. Acta* **1980**, *589*, 30.

(4) Koepke, J.; Hu, X.; Muenke, C.; Schulten, K.; Michel, H. *Structure* **1996**, *4*, 581.

(5) Prokhorenko, V. I.; Holzwarth, A. R.; Müller, M. G.; Schaffner, K.; Miyatake, T.; Tamiaki, H. *J. Phys. Chem. B* **2002**, *106*, 5761.

(6) Didraga, C.; Klugkist, J. A.; Knoester, J. *J. Phys. Chem. B* **2002**, *106*, 11474.
(7) Oostergetel, G. T.; Reus, M.; Gomez Maqueo Chew, A.; Bryant, D. A.; Boekema, E. J.; Holzwarth, A. R. *FEBS Lett.* **2007**, *581*, 5435.
(8) Tamiaki, H.; Amakawa, M.; Shimono, Y.; Tanikaga, R.; Holzwarth, A. R.; Schaffner, K. *Photochem. Photobiol.* **1996**, *63*, 92.
(9) Pawlik, A.; Kirstein, S.; DeRossi, U.; Dähne, S. *J. Phys. Chem. B* **1997**, *101*, 5646.
(10) von Berlepsch, H.; Böttcher, C.; Ouart, A.; Burger, C.; Dähne, S.; Kirstein, S. *J. Phys. Chem. B* **2000**, *104*, 5255.
(11) von Berlepsch, H.; Ouart, A.; Regenbrecht, M.; Akari, S.; Keiderling, U.; Schnablegger, H.; Dähne, S.; Kirstein, S. *Langmuir* **2000**, *16*, 5908.
(12) Didraga, C.; Pugžlys, A.; Hania, P. R.; von Berlepsch, H.; Duppen, K.; Knoester, J. *J. Phys. Chem. B* **2004**, *108*, 14976.
(13) Pugžlys, A.; Augulis, R.; van Loosdrecht, P. H. M.; Didraga, C.; Malyshev, V.; Knoester, J. *J. Phys. Chem. B* **2006**, *110*, 20268.
(14) Poderys, V.; Selskis, A.; Rotomskis, R. *Solid State Phenomena* **2004**, *97*−*98*, 221.
(15) Doan, S. C.; Shanmugham, S.; Aston, D. E.; McHale, J. L. *J. Am. Chem. Soc.* **2005**, *127*, 5885.
(16) Gandini, S. C. M.; Gelamo, E. L.; Itri, R.; Tabak, M. *Biophys. J.* **2003**, *85*, 1259.
(17) Rotomskis, R.; Augulis, R.; Snitka, V.; Valiokas, R.; Liedberg, B. *J. Phys. Chem. B* **2004**, *108*, 2833.
(18) Wang, Z. C.; Medforth, C. J.; Shelnutt, J. A. *J. Am. Chem. Soc.* **2004**, *126*, 15954.
(19) Wang, Z.; Medforth, C. J.; Shelnutt, J. A. *J. Am. Chem. Soc.* **2004**, *126*, 16720.
(20) Schwab, A. D.; Smith, D. E.; Bond-Watts, B.; Johnston, D. E.; Hone, J.; Johnson, A. T.; de Paula, J. C.; Smith, W. F. *Nano Lett.* **2004**, *4*, 1261.
(21) Ohno, O.; Kaizu, Y.; Kobayashi, H. *J. Chem. Phys.* **1993**, *99*, 4128.
(22) Pasternack, R. F.; Schaefer, K. F.; Hambright, P. *Inorg. Chem.* **1994**, *33*, 2062.
(23) Ribó, J. M.; Crusats, J.; Farrera, J.-A.; Valero, M. L. *J. Chem. Soc.: Chem. Commun.* **1994**, 681.
(24) Akins, D. L.; Zhu, H.-R.; Guo, C. *J. Phys. Chem.* **1994**, *98*, 3612.
(25) Maiti, N. C.; Ravikanth, M.; Mazumdar, S.; Periasamy, N. *J. Phys. Chem.* **1995**, *99*, 17192.
(26) Akins, D. L.; Zhu, H.-R.; Guo, C. *J. Phys. Chem.* **1996**, *100*, 5420.
(27) Zhang, Y.-H.; Chen, D.-M.; He, T.; Liu, F.-C. *Spectrochim. Acta Part A* **2003**, *59*, 87.
(28) Augulis, R.; Valiokas, R.; Liedberg, B.; Rotomskis, R. *Solid State Phenomena* **2004**, *97*−*98*, 195.
(29) Escudero, C.; Crusats, J.; Díez-Pérez, I.; El-Hachemi, Z.; Ribó, J. M. *Angew. Chem., Int. Ed.* **2006**, *45*, 8032.
(30) Augulis, R.; Sugonyko, A. V.; Pugžlys, A. unpublished data.
(31) Augulis, R.; Tamuliene, J.; Tamulis, A.; Rotomskis, R. *Solid State Phenomena* **2004**, *97*−*98*, 225.
(32) Stuart, M. C. A.; Boekema, E. J. *Biochim. Biophys. Acta*−*Biomembr.* **2007**, *1768*, 2681.
(33) Gouterman, M. *J. Mol. Spectrosc.* **1961**, *6*, 138.
(34) Fleischer, E. B.; Palmer, J. M.; Srivastava, T. S.; Chatterjee, A. *J. Am. Chem. Soc.* **1971**, *93*, 3162.
(35) Pasternack, R. F.; Huber, P. R.; Boyd, P.; Engasser, G.; Francesconi, L.; Gibbs, E.; Fasella, P.; Venturo, G. C.; de, L. *J. Am. Chem. Soc.* **1972**, *94*, 4511.
(36) Rotomskis, R. 2008, private communications.
(37) Didraga, C.; Knoester, J. *J. Chem. Phys.* **2004**, *121*, 10687.
(38) Rubires, R.; Farrera, J.-A.; Ribó, J. M. *Chem. Eur. J.* **2001**, *7*, 436.
(39) Bednarz, M.; Knoester, J. *J. Phys. Chem. B* **2001**, *105*, 12913.
(40) Zimmermann, J.; Siggel, U.; Fuhrhop, J.-H.; Röder, B. *J. Phys. Chem. B* **2003**, *107*, 6019.
(41) Yildirim, H.; Işeri, E. I.; Gülen, D. *Chem. Phys. Lett.* **2004**, *391*, 302.
(42) Gülen, D. *Photosynthesis Res.* **2006**, *87*, 205.
(43) Kelbauskas, L.; Bagdonas, S.; Dietel, W.; Rotomskis, R. *J. Lumin.* **2003**, *101*, 253.
(44) Hoard, J. L. In *Porphyrins and Metalloporphyrins*; Falk, J. E., Smith, K. M.; Elsevier: Amsterdam, 1975; pp 317−380.
(45) For N_i odd, the allowed values extend to $k_i = 0, \pm1, \pm2,. ., \pm(N_i-1)/2$.
(46) Davydov, A. S. *Theory of Molecular Excitons*; Plenum Press: New York, 1971.
(47) Briggs, J. S.; Herzenberg, A. *Mol. Phys.* **1971**, *21*, 865.
(48) These results are valid in the limit of long cylinders; minor additional peaks with $k_2 = \pm1$ may appear for smaller cylinders, even upon application of periodic boundary conditions; see ref 6.
(49) (a) Schreiber, M.; Toyozawa, Y. *J. Phys. Soc. Jpn.* **1982**, *51*, 1528. (b) Schreiber, M.; Toyozawa, Y. *J. Phys. Soc. Jpn.* **1982**, *51*, 1537.
(50) Fidder, H.; Knoester, J.; Wiersma, D. A. *J. Chem. Phys.* **1991**, *95*, 7880.
(51) Bakalis, L. D.; Rubtsov, I.; Knoester, J. *J. Chem. Phys.* **2002**, *117*, 5393.
(52) Soven, P. *Phys. Rev.* **1967**, *156*, 809.
(53) Taylor, D. W. *Phys. Rev.* **1967**, *156*, 1017.
(54) Economou, E. N. *Green's Functions in Quantum Physics*; Springer Verlag: Berlin, 1983.
(55) Note that the Green's function and thus the self-energy will still depend on the branch label *j*. We proceed with using the average over both branches; moreover, the difference between the effects of choosing either branch for the self-energy is small.
(56) Rubires, R.; Crusats, J.; El-Hachemi, Z.; Jaramillo, T.; López, M.; Valls, E.; Farrera, J.-A.; Ribó, J. M. *New J. Chem.* **1999**, *23*, 189.
(57) Pasternack, R. F.; Fleming, C.; Herring, S.; Collings, P. J.; dePaula, J.; DeCastro, G.; Gibbs, E. *Biophys. J.* **2006**, *29*, 550.
(58) (a) Heijs, D. J.; Malyshev, V.; Knoester, J. *Phys. Rev. Lett.* **2005**, *95*, 177402. (b) Heijs, D. J.; Malyshev, V.; Knoester, J. *J. Chem. Phys.* **2005**, *123*, 144507.
(59) (a) Lemaistre, J. P. *J. Lumin.* **1999**, *83*−*84*, 229. (a) Lemaistre, J. P. *J. Lumin.* **2004**, *107*, 332.
(60) Akins, D. L. In *J-Aggregates*; Kobayashi, T., Ed.; World Scientific: Singapore, 1996; pp 67−94.
(61) Eisfeld, A.; Kniprath, R.; Briggs, J. S. *J. Chem. Phys.* **2007**, *126*, 104904.
(62) Engel, G. S.; Calhoun, T. R.; Read, E. L.; Ahn, T. K.; Mancal, T.; Cheng, Y. C.; Blankenship, R. E.; Fleming, G. R. *Nature* **2007**, *446*, 782.
(63) Betzig, E.; Trautman, J. K. *Science* **1992**, *257*, 189.
(64) Gerton, J. M.; Wade, L. A.; Lessard, G. A.; Ma, Z.; Quake, S. R. *Phys. Rev. Lett.* **2004**, *93*, 180801.

JP808235C